In situ fabrication of hierarchically porous g-C$_3$N$_4$ and understanding on its enhanced photocatalytic activity based on energy absorption

Yudong Li[a,1], Zhaohui Ruan[b,1], Yanzhen He[c], Junzhuo Li[a], Kunqiao Li[a], Yanqiu Jiang[a,*], Xianzhu Xu[a], Yuan Yuan[b,*], Kaifeng Lin[a,d,**]

[a] *MIIT Key Laboratory of Critical Materials Technology for New Energy Conversion and Storage, School of Chemistry and Chemical Engineering, Harbin Institute of Technology, Harbin 150001, China*
[b] *Key Laboratory of Aerospace Thermophysics, Ministry of Industry and Information Technology, School of Energy Science and Engineering, Harbin Institute of Technology, Harbin 150001, China*
[c] *School of Chemistry and Pharmaceutical Engineering, Qilu University of Technology, Jinan 250353, China*
[d] *Key Laboratory of Advanced Energy Materials Chemistry (Ministry of Education), Nankai University, Tianjin 300071, China*

ARTICLE INFO

ABSTRACT

A novel strategy is proposed to *in situ* synthesize hierarchically porous g-C$_3$N$_4$ foam (FCN) with no carbon residue by low-cost polyurethane sponge as single template. The porous system consists of interconnected micron- (1–2 μm) and nano-scale (20–80 nm) pores, which is usually constructed tediously. For visible light catalysis, the FCN with unique hierarchical pores possesses higher efficiency for H$_2$ generation (8 times) and phenol degradation (4 times) over pristine g-C$_3$N$_4$ due to the increased BET surface area, accelerated mass transfer and improved efficiency of exciton generation and dissociation, which all derive from the hierarchical pore system. Further, an optical simulation is initially adopted to illustrate the effect of the hierarchical porosity with micron- and nano-scale pores on the ability of light absorption and penetration over FCN and an energy-absorption-based explanation is proposed to deeply explain the enhanced photocatalytic activity, which opens a window to directly understand the relationship of the enhanced photocatalytic activities and absorbed light energy increased by the hierarchical pores system.

1. Introduction

Photocatalysis is a promising technique for H$_2$ generation and pollutants degradation [1–10]. However, traditional photocatalysts are either toxic or inefficient, leading to numerous efforts to develop alternative ones [11–13]. Among them, graphitic carbon nitride (g-C$_3$N$_4$), a polymeric non-metal photocatalyst, is currently drawing attention due to its advantages such as chemical stability, easy preparation and visible light response [14]. Nevertheless, g-C$_3$N$_4$ still exhibits low photocatalytic efficiency stemming from its weak light absorption ability, low specific surface area, and fast recombination of photogenerated active charges [15,16]. Methods like heteroatom doping, semiconductor coupling, and pore creation have been employed to enhance catalytic performances of g-C$_3$N$_4$ materials [17–30], and the thin nanosheets are also prepared to improve the photocatalysis [31–33]. Among these strategies, pore creating has been considered to

be a simple and effective approach, by which the porous g-C$_3$N$_4$ possessing higher specific surface area, faster mass transfer and more efficient exciton dissociation have been successfully fabricated [34,35]. Porous silica can be used as hard duplicating template, and F127, P123, Triton X-100 and ionic liquid as soft sacrificial templates [36–39]. Without prejudice to the above, however, it has been noted that the hard template needed to be removed by using toxic corrodents containing F element and that organic soft templates would bring a high residual carbon after calcination [40], which may result in "shielding effect" diminishing the efficiency of light absorption and exciton dissociation, and covering the active sites, thus reduces catalytic efficiency [41]. Wherein the soft strategy, gas bubble-based method has been investigated to prepare porous g-C$_3$N$_4$ with no or less carbon residue. Unimodal pores contained in g-C$_3$N$_4$ materials have been obtained by using sublimed sulfur and urea as bubble templates respectively, and both of them exhibit superb catalytic performances [36,42].
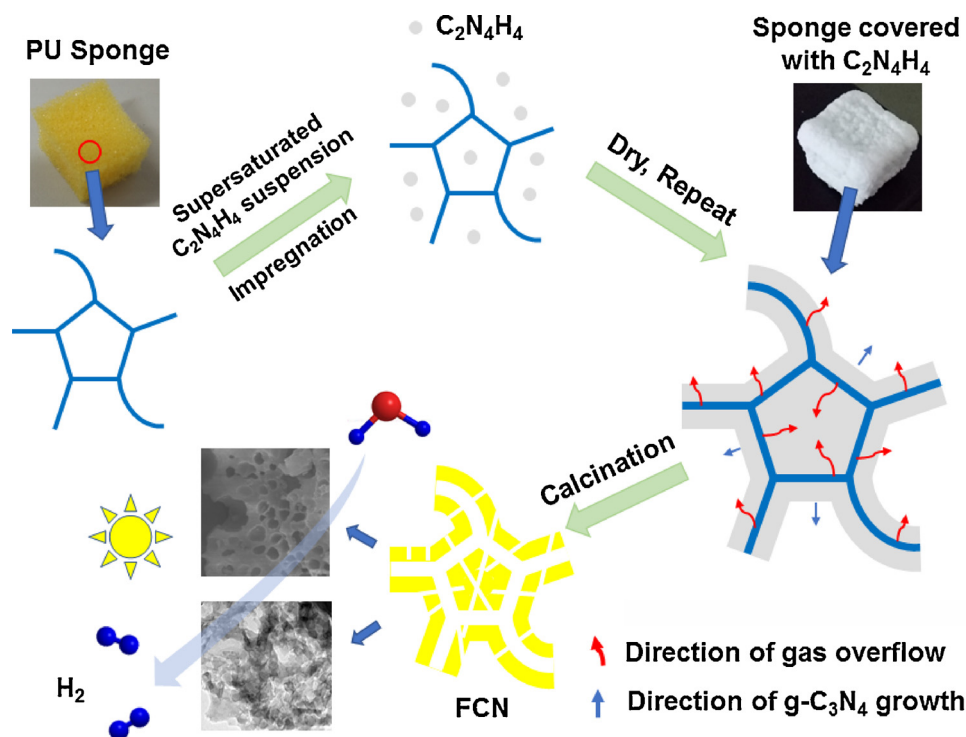
Fig. 1. Schematic for the preparation of FCN materials.

Design of a hierarchically porous system by possessing additional macropores into a mesoporous photocatalyst would improve the catalytic efficiency, by providing a "channel" to enhance mass transfer and thus improve the accessibility of the material and retard the deposition of products and poisoning of photocatalyst [34,43–45]. Moreover, the introduced macropores would transport light from the surface into the inner porous framework by multiple reflection, if the pore size is larger than the wavelength of light in photocatalysis. Thus the light energy is expected to be adequately utilized [46], which is the first step in photocatalysis converting light energy to chemical energy. Nevertheless, most of current researches focused on the other steps like exiton dissociation and mass transfer. The studies on light absorption generally cared the absorbed region, and little concerned the intensity, which would directly affect the amount of photo-generated active charges thus determine the catalytic performance [47]. It has been partly confirmed the modified porous structures can enhance the intensity of light absorption in previous works [48].

Generally, preparation of a hierarchically porous material needs dual- or triplex-template, which would be a relatively tedious and complicated process, and hierarchically porous g-C_3N_4 is hard to be synthesized due to its natural characters. Hence, it is of great interest to design a simple strategy to synthesize hierarchically porous g-C_3N_4, and it is meaningful and instructive to analyze the intensity of light absorption over hierarchically porous g-C_3N_4.

Polyurethane (PU) in soft format (no or less aromatic ring) is a common, cheap cleaning material produced industrially. The skeleton of PU sponge shrinks and decomposes completely into gases and sublimable/gasifiable small molecules before 500 °C [49,50]. Therefore, as a soft template in the preparation of porous materials, especially whose synthetic temperature coincide with the decomposed temperature of PU sponge, PU would not leave any impurities under suitable heating conditions, but *in situ* introduce micron-pores and nano-pores simultaneously. Melamine sponge would leave plenty of carbon residue leading to a low catalytic performance although possessed a high rigidity.

Herein, PU was initially employed as a sacrificial soft template to *in situ* synthesize hierarchically porous g-C_3N_4 foam (FCN), just by sintering the mixture of PU and dicyandiamide (DCDA, precursor of g-

C_3N_4). The hierarchical pores with nano-scale (20–80 nm) and micron-(1–2 μm) pores were constructed based on the following two considerations. One is the temperature for the condensation of g-C_3N_4 covering that for PU decomposition, and the other is the escaped decomposition gas products and the shrinkage of voids formed from escaped skeletons forming pores in different sizes. This strategy can reduce the amount of carbon residues, and the unique pore system possessed enhanced light absorption and penetration, improved mass transfer, BET surface area, and efficiency of exciton dissociation thus to increase the photocatalytic ability. Notably, an optical simulation was initially adopted to illustrate the effect of the hierarchical porosity with micron- and nano-scale pores on the ability of light absorption over the FCN and an energy-absorption-based explanation is proposed to explain the enhanced photocatalytic activity.

2. Experimental section

2.1. Materials

Dicyandiamide (DCDA) were purchased from Sinopharm Chemical Reagent Co., Ltd, and the cleaning sponge in soft polyurethane (PU) format (0.0358 g per 2 cm^3, BET is 3.785 m^2 g^{-1} and 1.27 ml water adsorbed per 1 cm^3) was purchased from Jinya Household Supplies Co., Ltd. The materials were used without further purification.

2.2. Preparation of hierarchical porous g-C_3N_4 foam

Hierarchical porous g-C_3N_4 foam (FCN) was *in situ* synthesized by simply calcining the PU sponge that had been adequately impregnated with aqueous DCDA suspension liquid. In a typical run shown in Fig. 1, pieces of soft cubic PU sponges (0.5 × 0.5 × 0.5 cm, any other suitable shapes can also be usable, no nylon and corundum existed) were impregnated in a supersaturated DCDA aqueous suspension liquid under a moderately stirring. Before impregnation, 30 min of stirring and supersonic for the solution was adopted to form a homogeneous white suspension liquid. After 1 h adsorption (fully removing the adherent air on PU), the remaining suspension liquid was decanted and the PU

sponges were dried at 60 °C. Then the treated PU sponges with DCDA on the skeleton were then repeatedly impregnated 3 times to adequately enrich the DCDA in PU sponge (denoted as PU-DCDA). In order to saturate the PU-DCDA with DCDA molecules, the PU-DCDA was further soaked in a supersaturated DCDA aqueous solution (1.2 ml per cube) at 60 °C until the liquid was evaporated completely. The hierarchically porous g-C_3N_4 foam (FCN) was finally obtained by sintering the PU-DCDA sponges in a muffle at 550 °C for 1 h (ramp of 5 °C min^{-1}). Different heating rates formed different FCN materials (FCN-1.5, -5 and -10 refers to heating rate of 1.5, 5 and 10 °C min^{-1}, respectively). The pristine g-C_3N_4 (PCN) was prepared by simply sintering the DCDA without PU as template, and PCN-1.5, PCN-5 (denoted as PCN under no special condition) and PCN-10 refer to the PCN prepared by different heating rates of 1.5, 5 and 10 °C min^{-1} respectively. PU heated at the rates of 1.5, 5 and 10 °C min^{-1} (denoted as PU-1.5, PU-5 and PU-10 respectively) were also prepared.

2.3. Characterizations

All the tests were illustrated in the supporting information in detail.

2.4. Photocatalytic reactions

The activity of photocatalysts was evaluated *via* H_2 generation (reduction reaction) and phenol degradation (oxidation reaction) under visible light (λ > 400 nm) irradiation. The photocatalytic H_2 generation was operated in a close glass system with carrying gas channels. Photocatalyst (100 mg) was dispersed in triethanolamine (TEOA, as a sacrificial agent) aqueous solution (300 ml, 10 vol %), Pt (1.5 wt %) was employed as co-catalyst generated from $H_2PtCl_6·6H_2O$. After 5 min sonication, the suspension system was evacuated to remove O_2 and inflated with N_2. A 300 W Xe lamp with a UV cutoff filter (λ > 400 nm) was chosen as the light source. The H_2 yield was examined and calculated on TCD. A series of band-pass filters (λ = 380, 420, 450, 500, 550 nm) were used to obtain monochromatic light. The apparent quantum yield (AQY) was calculated using the formula,

$$AQY = \frac{Number\ of\ hydrogen \times 2}{Number\ of\ incident\ photon} \times 100\% \tag{1}$$

For the phenol degradation, typically, photocatalyst (50 mg) was dispersed in phenol solution (50 ml, 10 mg L^{-1}) under stirring at room temperature. The light source was as same as for the H_2 generation and the reactor was a cylindrical flask with a circulating cooling water cell with thickness of 5.0 cm to remove IR beams thus to eliminate the impact of temperature. The dispersion was kept in dark for 1 h to reach adsorption and desorption equilibrium adequately between photocatalysts and phenol before irradiation. 1 ml of solution was collected in a constant interval during irradiation and analyzed using a UV–vis spectrophotometer, and the intermediates were detected by GC–MS. The pH of the investigated phenol approximated 6.9, which would not disturb the light absorption and not promote the self-degradation of phenol. The efficiency (%) of degradation was calculated by the following formulation,

$$Efficiency\ (\%) = \frac{(C_0 - C_{test})}{C_0} \tag{2}$$

Where C_0 was the original dye concentration and C_{test} was the remaining concentration of dye at each irradiation interval time.

2.5. Principles of optical absorption calculation

The FDTD simulation was performed on FDTD solutions software developed by the Lumerical company. The Maxwell's equations are as follows:

$$\nabla \cdot \mathbf{D}(t) = \rho(t) \tag{3}$$

$$\nabla \cdot \mathbf{B}(t) = 0 \tag{4}$$

$$\nabla \times \mathbf{E}(t) = -\frac{\partial \mathbf{B}(t)}{\partial t} \tag{5}$$

$$\nabla \times \mathbf{H}(t) = \mathbf{J}(t) - \frac{\partial \mathbf{D}(t)}{\partial t} \tag{6}$$

Where **D**, **E**, **H** and **B** represent the electric displacement vector, electric field intensity, magnetic field intensity and magnetic induction, respectively. **J** represents the current density.

The Poynting vector **S** was calculated as follows:

$$\mathbf{S} = \frac{1}{2} \operatorname{Re}(\mathbf{E} \times \mathbf{H}^*) \tag{7}$$

Where the **E** and **H** denote the electric field intensity and the magnetic field intensity, respectively.

The divergence of the Poynting vector **P** was calculated as follows:

$$\mathbf{P} = -\nabla \cdot \mathbf{S} \tag{8}$$

$$\mathbf{P} = -\frac{1}{2} \cdot \omega \cdot |\mathbf{E}| \cdot lmag(\varepsilon) \tag{9}$$

Where ω is the angular frequency of the light, ε is the permittivity which can be calculated from the refractive index **n** and the extinction coefficient **k**:

$$Real\ (\varepsilon) = \mathbf{n}^2 - \mathbf{k}^2 \tag{10}$$

$$lmag\ (\varepsilon) = 2 \cdot \mathbf{n} \cdot \mathbf{k} \tag{11}$$

3. Results and disscussion

3.1. Synthesis and morphology analysis of FCN materials

The strategy of preparing FCN materials follows the scheme in Fig. 1. PU sponges were mixed with supersaturated DCDA aqueous suspension under mild stirring. After being adequately impregnated, the mixture was dried and heated. During the following heating process, the sponges decomposed into gas micro-molecules and polyhydric and higher alcohols. Meanwhile, DCDA condensed into melamine and further tris-*s*-triazine and heptazine. The alcohols would decompose or volatilize during calcination, and the hierarchically porous g-C_3N_4 was finally *in situ* obtained by condensation of the tris-*s*-triazine and heptazine unit. Two considerations resulted in the hierarchically porous system, first is the polymerization temperature of g-C_3N_4 coinciding the decomposition temperature of PU, and second is the escaped decomposition gas products and the shrinkage of voids formed from escaped skeletons constructing pores with different sizes. Different heating rates were used to form different FCN materials. In Fig. S1, compared with the pristine g-C_3N_4 (PCN), all the FCN materials prepared *in situ* using PU as soft template exhibit dark appearances, which would absorb more light. As shown in Fig. S2, the colors of the pristine g-C_3N_4 prepared by different heating rates were quite the same, ruling out that colour change of samples was resulted by the heating rates.

The interior porous structure of FCN-5 was first investigated by SEM and TEM. Pristine g-C_3N_4 displays bulk morphology without any apparent pores in the SEM images (Fig. 2a). In contrast, FCN-5 possesses unique pores in the range of 1–2 μm (Fig. 2b, c and Fig. S3a and b), and a mass of mesopores around 50–100 nm in size (red circles in Fig. 2d). The nano-scale mesopores should be attributed to the escape of gases from the decomposition and vaporization of soft PU template, whereas micron-scale pores stem from shrinkage of the void created by burning out the PU bone fibers (Fig. 2e) during heating process. Compared with the smooth layers in PCN (Fig. 2f), the TEM image of FCN-5 displays porous structures with pore size at 20–100 nm (red arrows in Fig. 2g and h, and Fig. S3c and d), which should derive from the soft PU template and gas bubbles. The introduced micron-scale pores into the nano-scale porous g-C_3N_4 material would assist visible light penetration
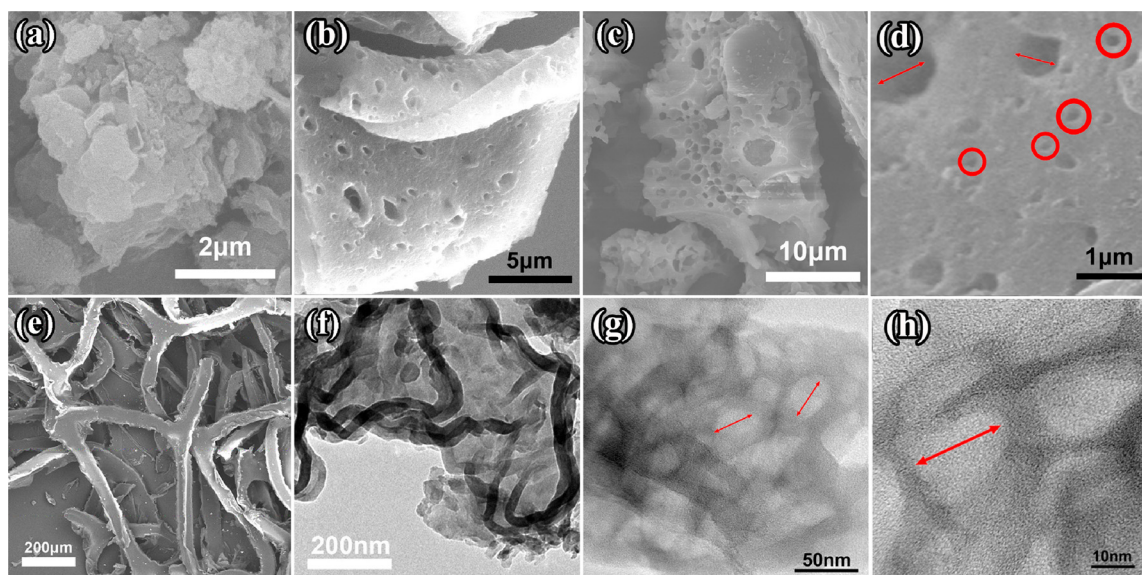
Fig. 2. SEM images of (a) PCN, (b, c, d) FCN-5 and (e) PU sponge. TEM images of (f) PCN and (g, h) FCN-5, the red arrows in (d) refer to the micron-scale pores, the red circles in (d) and the red arrows in (g) and (h) refer to nano-scale pores (For interpretation of the references to colour in this figure legend, the reader is referred to the web version of this article).

and absorption, and favor the transfer of reactants within the pores of FCN, thus improves the photocatalytic performance.

The N$_2$ adsorption-desorption isotherms of FCN materials are all of type IV with H3 hysteresis loops (Fig. S4), confirming the existence of abundant large-scale mesopores and/or macropores. Typically, FCN-5 possesses a larger BET surface area (58.7 m^2 g^{-1}, Table S1) and a higher pore volume (0.57 cm^3 g^{-1}) than PCN (6 m^2 g^{-1} and 0.12 cm^3 g^{-1}). The pore size distribution of FCN displays a wide peak at 20–80 nm (Fig. 3a), which accords with the SEM and TEM images. Owing to the fast heating process, FCN-10 possesses a larger BET surface area (64.5 m^2 g^{-1}) stemming from defects and pores created during polymerization. However, its lower pore volume (0.31 cm^3 g^{-1}) and smaller pore size (32 nm) imply that the pores are somewhat occupied by certain material. FCN-1.5 displays a lower BET surface area (32.4 m^2 g^{-1}) and pore volume (0.28 cm^3 g^{-1}), possibly because PU completely decomposed and vaporized before the full polymerization of g-C$_3$N$_4$ at the slow heating rate. By mercury intrusion porosimetry (MIP) characterization (Fig. 3b), the pore size distribution of micron-scale pores is centred at 1000–2500 nm, which is well in accordance with the SEM results.

Both TEM images and N$_2$ adsorption-desorption isotherms confirm the presence of the large mesopores and macropores in FCN-5. As reported previously, PU could decompose into gas micro-molecules and polyhydric alcohols and the alcohols would further decompose or volatilize during the heating process (Fig. S5) [49]. Thermogravimetry (TG) tests were adopted to illustrate the decomposition mechanism of PU. As shown in Fig. S6a and S7, PU-1.5 and PU-5 possess obvious decomposition curves with nearly zero residues. Hence, PU could be a potential soft template to *in situ* synthesize porous g-C$_3$N$_4$ without any residue. It can be concluded that during the condensation of DCDA into melamine and tris-*s*-triazine, the large mesopores and macropores are created by the gas molecules decomposed from PU template (Fig. S8). Besides, SEM images and MIP result clearly show that FCN-5 possesses unique pores in the micron-scale (1–2 μm). These pores might be attributed to the shrinkage of the voids formed from PU skeleton after it decomposed and vaporized during heating process. It is worth noting here that based on the creation mode of the nano- and micron-scale pores, these nano-scale pores are interconnected with the micron-scale pores to construct a hierarchical pore system, which would play an important role in photocatalytic reactions by improving the mass transfer and depth of light penetration, and enhancing the ability of light absorption and the separation of photo-generated active charges.

Based on TG analysis, it can be also observed that a small amount of carbon residue with low density exists when PU is heated at 10 °C min^{-1} (PU-10). Furthermore, the TG curve of mixed PU and DCDA under N$_2$ atmospheres displays two-step weight loss (Fig. S6b).
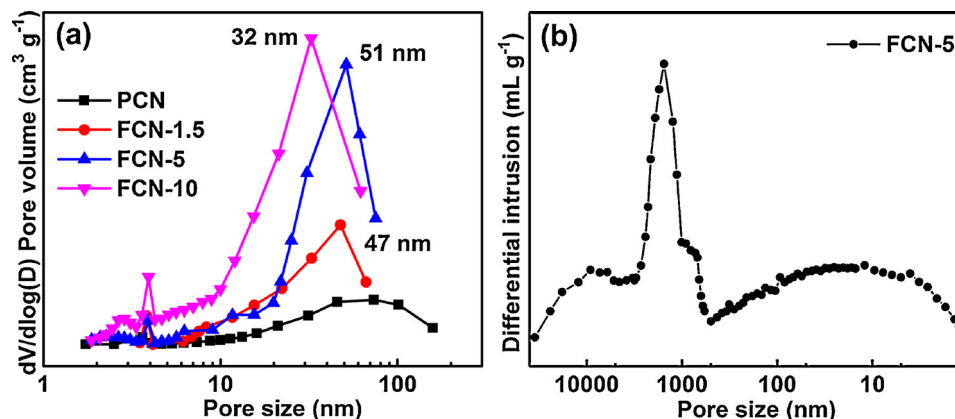
Fig. 3. (a) Pore size distribution curves of PCN and FCN materials by N$_2$ sorption, (b) pore size distribution of FCN-5 by mercury intrusion porosimetry (MIP).
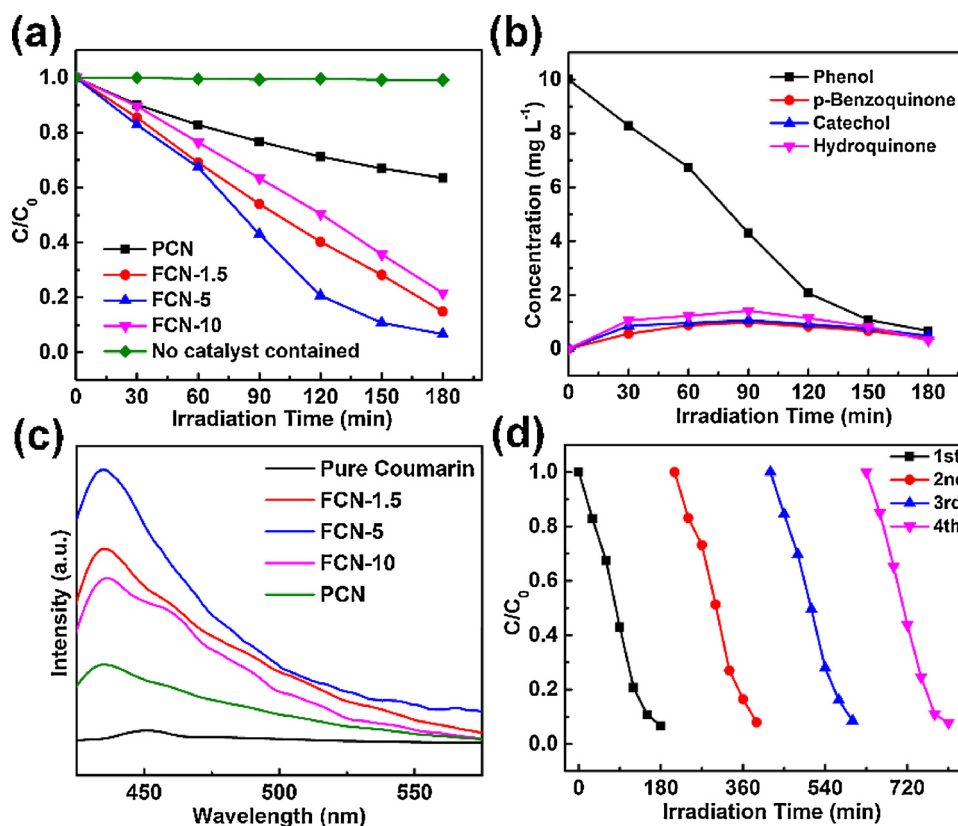
Fig. 4. (a) Photodegradation of phenol over PCN and FCN materials, (b) intermediates over FCN-5, (c) hydroxyl radical amount-related fluorescence spectra over PCN and FCN materials and (d) cyclic test over FCN-5 under visible light irradiation.

The first mass drop ($\sim$220–400 °C) belongs to the decomposition of PU and the pre-synthesis of g-C$_3$N$_4$ body-structure using DCDA. That is, the release of gases and organics (e.g. alcohols) results in the formation of nano- and micron-scale pores after vaporization and shrinkage while DCDA forms the blocks. A mild drop between 400–600 °C is ascribed to the polymerization of g-C$_3$N$_4$ and further decomposition of PU. It is worth noting that the thermograms of mixed PU and DCDA under air atmosphere gives similar platform as that under N$_2$ atmosphere, implying that this strategy can be used in different gases.

3.2. Characters of FCN materials

X-ray diffraction (XRD) was employed to illustrate the changes of interplanar spacing, which would affect the catalytic activity. FCN materials and PCN display similar peak positions at around 13° and 27° (Fig. S9), indicating the basic structure of g-C$_3$N$_4$ [51,52]. However, the peak at 27.5° in FCN-5 slightly shifted from that in PCN (27.3°). According to the Bragg formula, this corresponds to a reduction in interplanar spacing (d) from 0.326 to 0.324 nm [53]. This shrinkage should be attributed to the introduction of PU template and interference by the decomposition products, as proved by the XRD patterns of FCN-1.5, in whose case, no obvious shift appears at 27.3° since most of the template was consumed before the skeleton of g-C$_3$N$_4$ was thoroughly formed. Another piece of evidence is the shift of the (002) peak in the pattern of FCN-10, which should be ascribed to the carbon residue attaching to the walls of the pores, leading to a "confined growth effect" that causes the weak shift at (002) crystal face [48]. Moreover, the disappearance of the PU sponge peak at around 20° proves that there was no residual template or carbide. The C/N ratios of FCN materials were investigated by elemental analysis results (Table S2) and it was found that the C/N ratio of FCN-1.5 and FCN-5 is 0.67 and 0.68, similar as other porous g-C$_3$N$_4$ materials synthesized by hard and/or soft templates. This illustrates the existence of pores (or defects) and absence of residual PU in

the case of FCN-5. The slightly higher C/N ratio in FCN-10 (0.70) should be ascribed to the carbon residue from PU and/or the loss of $-$NH$_x$ during the fast heating procedure.

The XPS tests were employed to further examine the influence of different heating programs on the composition and inner structure of prepared FCN materials. All the FCN materials and PCN display similar peak positions in the C1s and N1s spectra (Fig. S10). Hence, there is no obvious change of FCN materials in the molecular level. The peaks at 284.4, 286.2, and 288.0 eV in C1s spectra correspond to C$-$C, C$-$NH$_x$ and N$-$C$=$N, and those at 398.7, 399.7, and 401.0 eV in N1s spectra correspond to C$-$N$\equiv$C, N$-$(C)$_3$, and $-$NH$_2$, respectively [22,54,55]. The area ratio between C–NH$_x$ (terminal, Fig. S11) and N$-$C$=$N is 0.008 in PCN (Table S3). Nevertheless, by using PU as template, this ratio rises remarkably to 0.035 (FCN-1.5), 0.071 (FCN-5), and 0.055 (FCN-10), implying more defects and pores existed. The content of C$-$C in FCN (0.20) is similar to that in PCN (0.19). This content decreases to 0.12 in FCN-5 and increases to 0.26 in FCN-10, suggesting that a large amount of residual C and/or doped C atoms exist in FCN-10. The utilization of PU with a suitable heating program can optimize the structure, because the C$-$C is not an important site for visible light response whereas tris-s-triazine and heptazine are. For the N species, the ratios between C$-$N$=$C and N$-$(C)$_3$ in FCN-1.5 (1.45) and FCN-5 (1.60) are similar to that in PCN (1.43). However, it decreases to 1.01 in FCN-10 due to the doping and/or decomposition. The ratio of $-$NH$_2$ increases from 0.03 in PCN to 0.09 in FCN-5, which illustrates the existence of defects and pores when using PU as template. Moreover, the $-$NH$_2$ group can improve the hydrophilicity, thus enhance the mass transfer [56]. The presence of terminal groups of $-$NH$-$ and $-$NH$_2$ (Fig. S11) in FCN materials was confirmed by FTIR spectra (Fig. S12a), displaying the peaks at around 3200 cm^{-1} [57]. As shown in Fig. S12b, the disappearance of the peaks at $\sim$1080 cm^{-1} assigned to C$-$O$-$C stretching vibration in the FTIR of PU confirms the complete decomposition of PU templates.
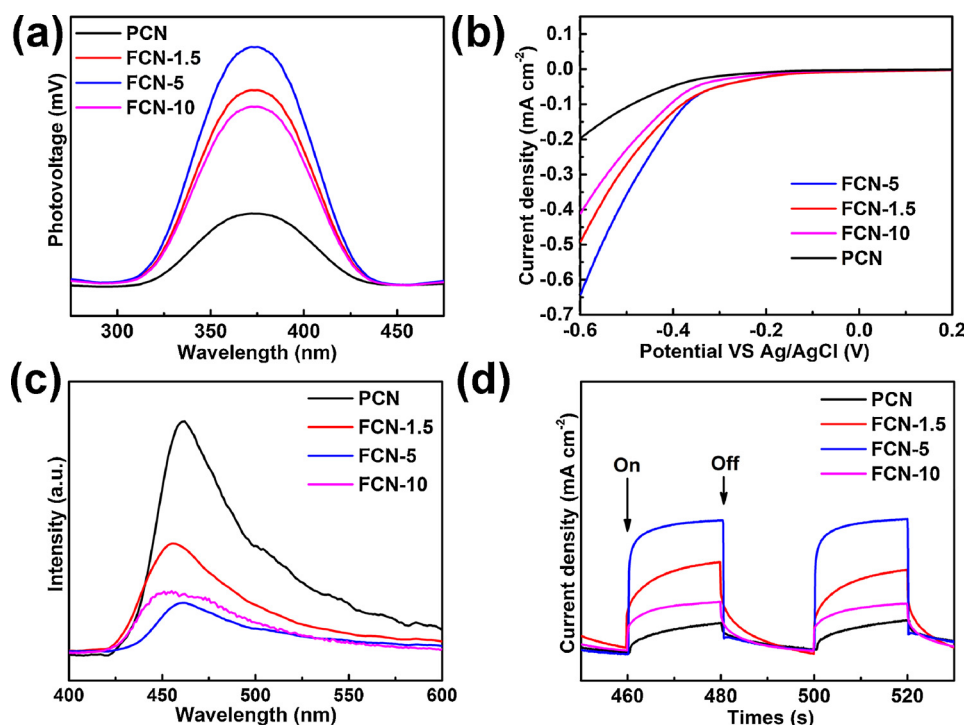
Fig. 5. (a) SPS peak intensities at air atmospheres, (b) PEC I–V curves under visible-light irradiation, (c) photoluminescence spectra and (d) periodic on/off photocurrent response of PCN and FCN materials under visible light irradiation.

3.3. Visible light catalytic characterization

Phenol is a kind of deleterious and refractory intermediate in the degradation of aromatic organics, meanwhile, it could ignore the interference from self-sensitization of dyes. With micron-scale and nano-scale pores introduced into the g-C_3N_4 bulk, FCN-5 exhibited excellent photocatalytic performance in phenol degradation. Before irradiation, 30 min dark adsorption was employed to reach the sorption equilibrium of phenol (Fig. S13a). Higher adsorption amounts of phenol were observed on FCN materials than that of PCN due to the presence to mesopores in FCN, which also implies the improved mass transfer of the substrates in FCN materials. For photodegradation, phenol owns a stable existence in the absence of catalyst under visible light irradiation (Fig. 4a), whereas rapid degradations appear with the utilization of PCN or FCN materials. Obviously, FCN-5 possesses the most efficient photodegradation, 93.4% of phenol was degraded over FCN-5 in 180 min while 85.1% over FCN-1.5, 78.4% over FCN-10 and 36.5% over PCN. The time for phenol photodegradation over FCN-5 is shorten 2/3 times compared with that over PCN. In comparison, FCN-1.5 and FCN-10 displayed lower degradation efficiencies ascribed to the lower pore volume and "shielding effect" respectively. The dynamics of degradation over different catalysts are shown in Fig. S13b, and the pseudo-first-order kinetics could be adopted to illustrate the curves,

$$\ln \frac{C_0}{C_{test}} = k \cdot t \tag{12}$$

where t is the irradiation time (min) and k is the rate constant (min^{-1}), which display approximate 2–5 times higher photocatalytic efficiency over FCN materials than over PCN. The superb performance should be attributed to the hierarchical pores system and lower carbon residue.

The phenol is degraded to small inorganic molecules, CO_2 and H_2O gradually, as proved by the concentration changes of intermediates and total organic carbon (TOC). Three main intermediates were detected by GC–MS, *i.e.* hydroquinone, catechol and p-benzoquinone, whose concentrations are shown in Fig. 4b. The contents of three intermediates decrease after a mild increment, which should be ascribed to the ring

cleavage process stemming from the attack of ·OH. A simple degradation process is shown in Fig. S13c, the phenol is first hydroxylated to the hydroquinone, catechol and p-benzoquinone, then these three intermediates turn into organic acids and finally mineralized into CO_2 and H_2O. Furthermore, TOC depicted in Fig. S13d illustrates that the degradation of phenol over FCN-5 is photo-mineralization rather than simple photo-bleaching, and 86.2% of TOC is removed in 180 min by using FCN-5 as visible light catalyst.

This superb mineralization ability of FCN-5 should be attributed to the large amount of ·OH generated by the photo-generated active charges moving rapidly to the surface. An easy method was employed to evaluate the contents of ·OH which is through the luminescent detection of the 7-hydroxycoumarin produced by the combination of coumarin and ·OH [58]. As shown in Fig. 4c, the photoluminescence (PL) intensity of the tested solution containing FCN-5 is the strongest one, which illustrates the yield of ·OH is highest over FCN-5 under visible light irradiation. FCN-1.5 and FCN-10 still exhibit relative higher PL intensity than that of PCN, which demonstrates that the incorporation of hierarchical pores play more important role in influencing the catalytic performances. Meanwhile, after 4 experimental cycles, the performance of FCN-5 for phenol degradation is still high (Fig. 4d), suggesting PCN-5 possesses a stable degradation ability. After the cycle tests, FCN-5 exhibits similar characters as before the tests, according to the N_2 adsorption-desorption, XRD, FTIR, UV–vis DRS and PL data in Fig. S14, further illustrating its outstanding stability.

3.4. Optical characters and optical simulation of FCN materials

Except for the improved mass transfer, FCN materials also possess strong photo-generation capacity of holes and electrons and high efficiency of charge separation, which are all attributed to the introduction of micron-pores into the nano porous system. As proven by surface photo-voltage spectroscopy (SPS, Fig. 5a), which derives from the photo-generated active charge separation over a nano-scale semiconductor and is an accepted measurement to evaluate the properties of photo-generated charges of solid semiconductor materials [58].

Notably, the intensity of PCN is low even in air atmosphere, in which the adsorbed O_2 owns a strong trapping ability of photo-generated electron thus resulting in a high efficiency of active charges separation. On the contrary, after introducing the hierarchical pores, the SPS signals of FCN materials possess positive amplifications, indicating a strong generation and separation efficiency of active charges. As expected, FCN-5 exhibits the highest signal amplification, attributing to the abundant hierarchical pores and low content of carbon shelters, and adversed structures would restrict the enhancement of SPS signal over FCN-1.5 and FCN-10 respectively. The SPS results illustrate the FCN materials especially FCN-5 possess higher generation and separation efficiency of active charges which are benefit to the photocatalytic performance.

To further illustrate the superb active charges separation efficiency over FCN materials, the photo-electrochemical I–V curves were also measured under visible-light irradiation in 0.5 M Na_2SO_4 solution. It can be observed that the PCN exhibits a relatively low current density at the same voltage (Fig. 5b), on the contrary, the current density of FCN materials deeply enhanced by incorporated with hierarchical pores at the same voltage. Obviously, FCN-5 possesses the highest amplification of current density, illustrating a fast charges separation existed. The enhancement should be attributed to sufficient pores and low carbon attachment, and similar like SPS results, the reversed former limits FCN-1.5 and the reversed latter limits FCN-10 in the enhancement of current density.

The pores also contribute to the enhanced photocatalytic activity by reducing the recombination of photo-generated active particles, as confirmed by PL and surface photocurrent measurements. As shown in Fig. 5c, the FCN materials display similar PL spectra to the PCN. However, the lower relative PL intensity of FCN materials demonstrates that the efficiency of separation between photo-generated holes and electrons is sharply increased. As a consequence, as soon as the light is turned on, the current generated on the surface of FCN materials and PCN all rise rapidly (Fig. 5d) [59]. However, the current intensity over FCN is higher than that over PCN, suggesting there are more available electrons in FCN, and this phenomenon accord with the results of ·OH capture experiment.

To illustrate the influence on the efficiency of exciton dissociation under different wavelength, photocurrent action spectra of FCN-5 and PCN was further measured under monochromatic light irradiation (Fig. S15) [60]. The curve of PCN remains unchanged in the > 450 nm wavelength range, suggesting the "photoelectric effect" occurs below 450 nm over PCN. Nevertheless, a distinct region and amplification appears in photocurrent action over FCN-5, whose obvious amplification located at 500 nm, and a decipherable enhancement at 550 nm. Furthermore, compared with PCN, an obviously reduced semicircle in the electrochemical impedance spectra (EIS) of FCN-5 was measured under light irradiation (Fig. S16), pointing to faster interfacial charge transfer in FCN-5. Interestingly, different variation trends appear by different materials. As the Raman spectra shown in Fig. S17, no graphitic carbon exists in PU-10, indicating a relatively weak conductivity of PU-10, although stronger than FCN-5 in dark. As soon as the light on, a slight variation of EIS semicircle over PU-10 appears, which should be attributed to the irremovability and fast recombination of photo-generated active charges due to the lack of π conjugated system [61,62]. Nevertheless, the EIS radius of FCN-5 decreases under irradiation even exceed that of PU-10, which demonstrates more removable electrons existed in the excited FCN-5, ascribing to the better activity under visible ligh irradiation.

The above-mentioned characterization results support that the hierarchical pores can not only accelerate the mass transfer, but also shorten the distance of the active particles moving to reach the surface, thus improving the photocatalytic performance by retarding the recombination between the active charges.

Generally, photocatalytic reaction over a semiconductor can be regarded as an energy conversion process, where light energy is

transformed into chemical and thermal energy [63–69]. Therefore, the ability of optical absorption determines the photocatalytic activity in some degree. In terms of nano-scale photonics, the near-field effect appears when the size of the interior structure of the photocatalyst is close to the wavelength of the incident light. Such near-field effect causes specific optical phenomena that geometrical optics cannot explain or be applied to [70]. Fortunately, the electrical field distribution based on electromagnetic optics can solve this problem. As a substitute, the optical simulation is a mostly used analyzing method by solving the governing equations of the optics [71]. According to current electromagnetics theories, the light is a kind of electromagnetic wave and its governing equations are also the Maxwell's equations composed of a series of partial differential equations presented in experimental sections, which are very difficult to be solved analytically [72]. Fortunately, many numerical methods like finite difference time domain (FDTD) methods, rigorous coupled wave analysis (RCWA), transfer matrix method (TMM) have been proved effective and widely applied in the optics [73,74]. Based on the simulations, the optical characteristics of the photocatalyst can be obtained (especially the electric field intensity distribution characteristics), from which the optical absorption characteristics can be further calculated with the optical properties of the materials. Nano-scale optical simulation was adopted to evaluate the optical characteristics of the interior structure of the photocatalyst, and to explain the enhanced photocatalytic activity in terms of light energy absorption.

For FCN-5 with hierarchical pores, its main distinguishing feature from other nano-porous g-C_3N_4 materials is the presence of many micron-scale pores. Therefore, the main task is to analyze the influence of these micron-scale pores on the light energy absorption characteristics. The model in Fig. 6a is adopted in the optical simulation, in which the nano-scale pores branch out perpendicularly from the micron-scale pores at uniform distances. The wavelength of the incident light is set to be 390 nm, and the periodic boundary condition is used. The electric field intensity distribution orthogonal to the direction of the incident light is shown in Fig. 6bi. To further distinguish the influences from the micron- and nano-scale pores on light absorption, materials with the micron-scale pores filled with pristine g-C_3N_4 were also simulated (Fig. 6bii). Comparing Fig. 6bi and bii, the micron-scale pores were found to facilitate the light transport into the nano-scale pores and subsequently enhance the optical absorption of the material. Next, to study the effects of the nano-scale pores, the optical characteristics are also calculated for the case with the nano-scale pores filled. The result (Fig. 6biii) illustrates that the nano-scale pores can enhance the light transport into the walls of the micron-scale pores. Finally, the electric field intensity distribution in the pristine g-C_3N_4 with no pores was calculated (Fig. 6biv). Comparing these results to Fig. 6bii, the micron-scale pores can also help to transport light more deeply into the photocatalyst.

Based on the electric field intensity distribution results that denote the different optical intensity inner the photocatalyst, the optical absorption characteristics can be straightforward obtained. According to electromagnetic theory, the energy flux density of the electromagnetic field can be expressed using the Poynting vector S (experimental section), thus the optical absorption power can be obtained with the divergence of the Poynting vector P (experimental section). With the optical absorption intensity, the generation rate of the photoinduced carriers thus can be evaluated from following formulas:

$$G = \frac{\lambda}{hc} \cdot \frac{P_{abs}(\lambda)}{P_{in}(\lambda)} I_{AM} 1.5(\lambda) \tag{13}$$

Where λ is the wavelength, h is the Plank's constant, c is the speed of light in the free space and $I_{AM}1.5$ is AM 1.5 solar spectrum which can be obtained from the website "http://rredc.nrel.gov/solar/spectra/am1.5/ASTMG173/ASTMG173.html". $P_{abs}(\lambda)$ is the optical absorption power at the wavelength λ, $P_{in}(\lambda)$ denotes the power of the incident light at wavelength λ. With which the photoinduced carrier
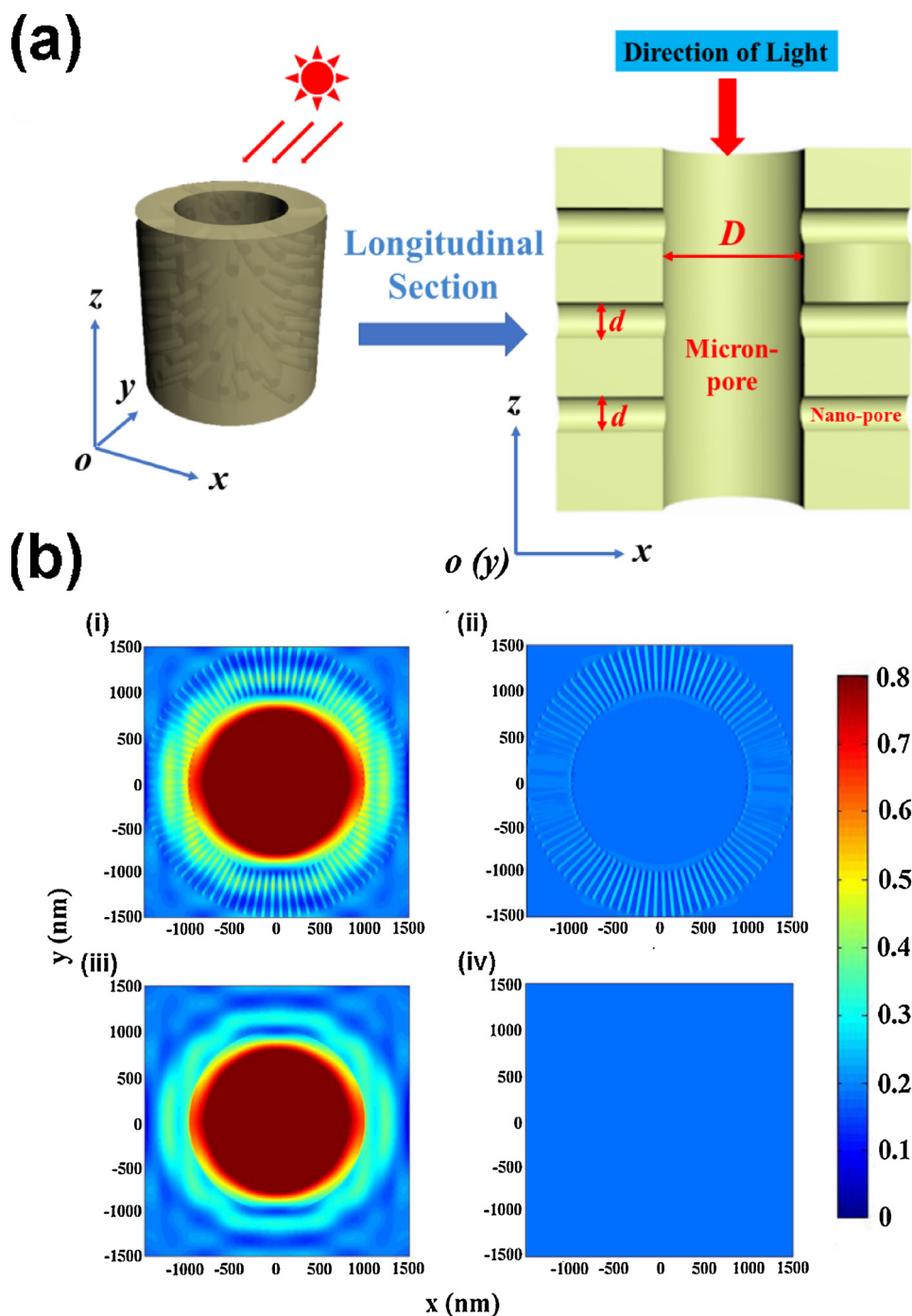
Fig. 6. (a) Simulation model of FCN materials. *D*: micron-pore diameter, *d*: nano-pore diameter and (b) distribution of electrical field in (i) FCN materials, (ii) FCN materials with nano-pores filled, (iii) FCN materials with micron-pores filled, and (iv) FCN materials with all pores filled.

generation rate can be calculated and the results are shown in Fig. S18. One can conclude that the enhancement of optical absorption of the photocatalyst can increase the generation rate of the photoinduced carriers and thus could get the photocatalytic activity enhanced.

Regarding the mechanism of enhancement in terms of light absorption, the UV–vis diffuse reflection spectrum (DRS) results give a further evidence that FCN materials have higher light absorption abilities than PCN, as well as expanded absorption regions to around 550 nm (Fig. 7a), confirming that the hierarchical pore architecture is indeed beneficial to the light absorption. Moreover, the curve thresholds of FCN materials are all higher than that of PCN, suggesting the former all have smaller band gaps (Fig. S19) [75]. This further confirms

that FCN materials can absorb visible light in a wider range. FCN-5 possesses a medium increment, and FCN-10 displays a wider range of absorption in the visible light region ascribing to the carbon residue, which, nevertheless, leading to a "shielding effects" which inhibits the exciton dissociation and the catalysis [41]. The narrower absorption range in FCN-1.5 should be attributed to the lack of pores in its inner structure. Thus, the mechanisms of the enhanced photocatalytic activity in terms of light absorption with micron- and nano-scale pores include two aspects. On one hand, the micron-scale pores can facilitate light transport into the nano-scale pores and deeper light penetration into the photocatalyst. Meanwhile, the nano-scale pores can also enhance the optical absorption on the pore walls and expand the visible light
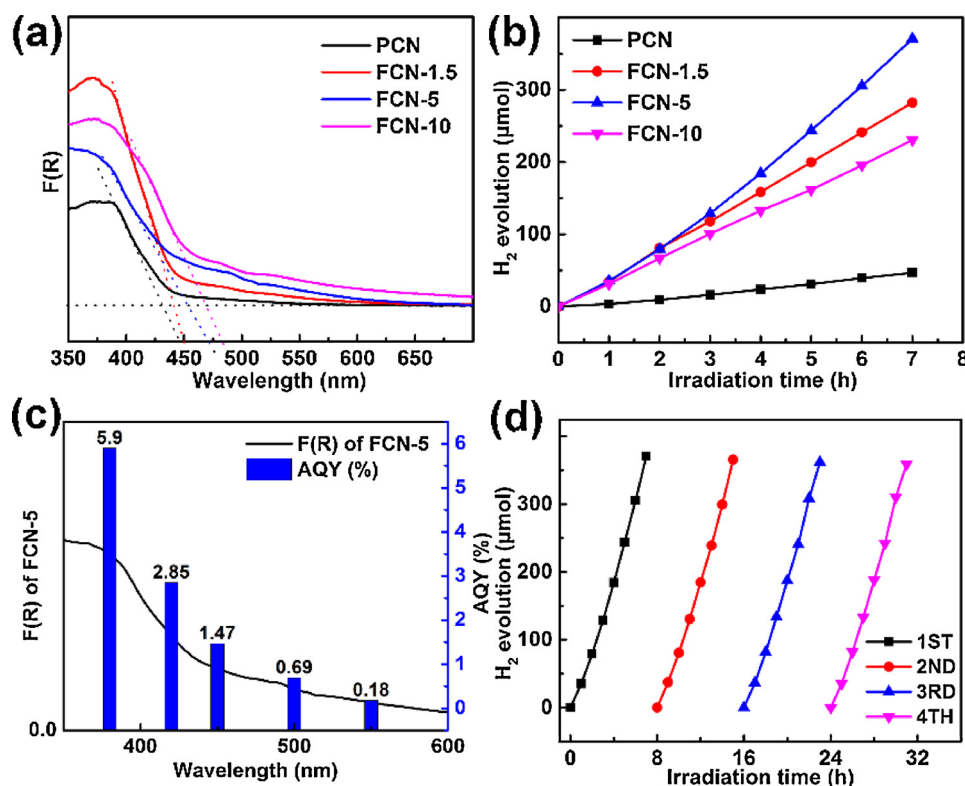
Fig. 7. (a) UV–vis absorption spectra, (b) photocatalytic H_2 generation over PCN and FCN materials, (c) AQY for FCN-5 under different monochromatic lights irradiation and (d) cyclic test of H_2 generation over FCN-5 under visible light irradiation ($\lambda > 400\,nm$).

absorption region [76]. These two factors determine the high light absorption of the hierarchically porous g-C_3N_4.

Based on the above-mentioned characterization results, both the micron- and nano-scale pores help to enhance the mass transfer and accessible reaction areas, and to reduce the recombination of photo-generated active particles. Especially, the micron-scale pores provide an expedite "channel" for light penetration into the interior of bulk g-C_3N_4, and the connected nano-scale pores enhance the light absorption. Consequently, FCN-5 has significantly improved photocatalytic performance. To illustrate the function of the micron-scale pores, FCN-5 was ball-milled to repeat the characterization and photocatalytic reaction. As shown in Fig. S20, the ball-milled FCN-5 sample remains the nano-pores and g-C_3N_4 structure (SEM and XRD), and the BET surface area ($56.9\,m^2\,g^{-1}$) and pore size distribution ($49\,nm$) of FCN-5 after ball-milling keep pace with those of FCN-5. However, the photocurrent and radius of EIS under visible light irradiation diminish after ball-milling, indirectly suggesting that the micron-pores could enhance the light absorption. As for the photodegradation shown in Fig. S21, ball-milled FCN-5 with few micron-scale pores possesses decreased catalytic activity, showing the importance of micron-scale pores.

With the introduction of hierarchical pores, FCN materials also exhibit excellent performance in H_2 generation. As shown in Fig. 7b, the rate of H_2 generation over FCN-5 is $59\,\mu mol\,h^{-1}$, which is about 8 times of that over PCN ($7\,\mu mol\,h^{-1}$). Moreover, after 4 consecutive reaction cycles, FCN-5 showed no obvious reduction in the rate and total amount of H_2 generation (Fig. 7c). Compared with that of FCN-5, the performance of FCN-1.5 for H_2 generation decreases remarkably because of its lower pore volume. Similar low performance observed for FCN-10 stems from the residual carbon, which diminishes the effective absorption of light over catalyst, covers the active sites and sacrifices the active charges supposed to be utilized in photocatalysis due to the "shielding effect" [41]. To further evaluate the photocatalytic activity of FCN-5, apparent quantum yield (AQY) under monochromatic light irradiation (Fig. 7d) is measured and is 2.85% with the utilization of

1.5% Pt and 3.91% with 3% Pt at 420 nm, which are better than that over PCN (Fig. S22). The AQY values accord with the photocurrent and UV–vis DRS results well. Compared some kinds of porous g-C_3N_4 [48,77–79], the hierarchically porous system indeed promote the photocatalytic performance. Notably, the FCN-5 displays a reduced catalytic performance in H_2 generation and AQY after ball-milling (Fig. S23, Table S4), which further demonstrates the importance of the created micron-sized pores.

Some controlling experiments were carried out to further explore the mechanism of H_2 generation and phenol degradation. As demonstrated above, the ·OH examined by coumarin is the active species in phenol degradation. Nevertheless, ·OH is not the only oxidizing substance confirmed by a series experiments to determine the active species in phenol degradation. By N_2 bubbling, the O_2 is eliminated, leading to a decrease in the efficiency of degradation from 93.4% to 47.1% after 3 h irradiation (Fig. 8a), which illustrates the existence of O_2 promotes the phenol degradation over FCN-5. The O_2 capture the photogenerated electrons to generate ·O_2^-. Furthermore, another three scavengers, benzoquinone (BQ, for superoxide radical (·O_2^-)), tert-butyl alcohol (TBA, for hydroxyl radical (·OH)) and triethanolamine (TEOA, for hole (h^+)) were added into the photocatalytic system respectively [80–82], and the degradation efficiencies are 35.5% (BQ), 76.1% (TEOA) and 64.3% (TBA) respectively. These results demonstrate that ·O_2^- is the major active species in the phenol degradation over FCN-5. However, ·O_2^- is a mild oxidant leading to cleavage rather than deep mineralization, combined with the weaker reductions appearing after injecting the TEOA and TBA, a conclusion can be gained · OH and h^+ are the essential active species although not the major ones. The mechanism of H_2 generation over FCN-5 is quite different from phenol degradation. As proved in Fig. 8b, the photo-generated electrons directly reduce the H^+ to H_2 over FCN-5, since that little H_2 is generated without catalyst, and the rate increases fast by adding FCN-5, and after adding $K_2S_2O_8$ as the electron scavenger, a sharp decrease appears in H_2 generation.
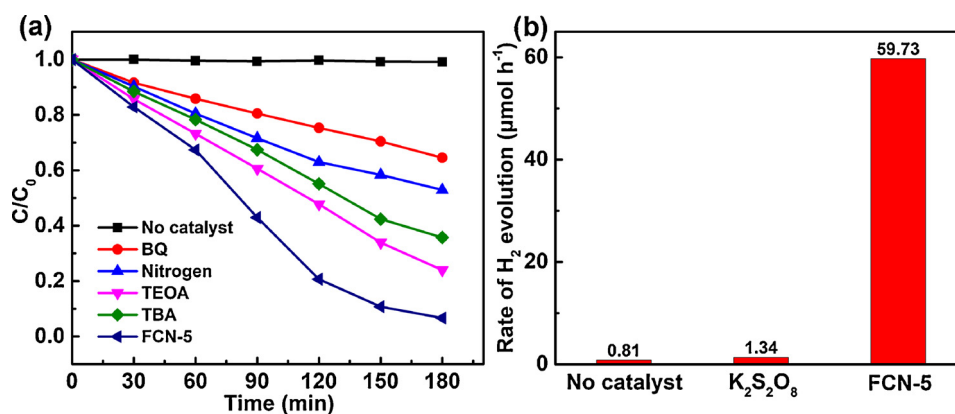
Fig. 8. (a) phenol degradation and (b) H_2 generation under different photocatalytic systems.
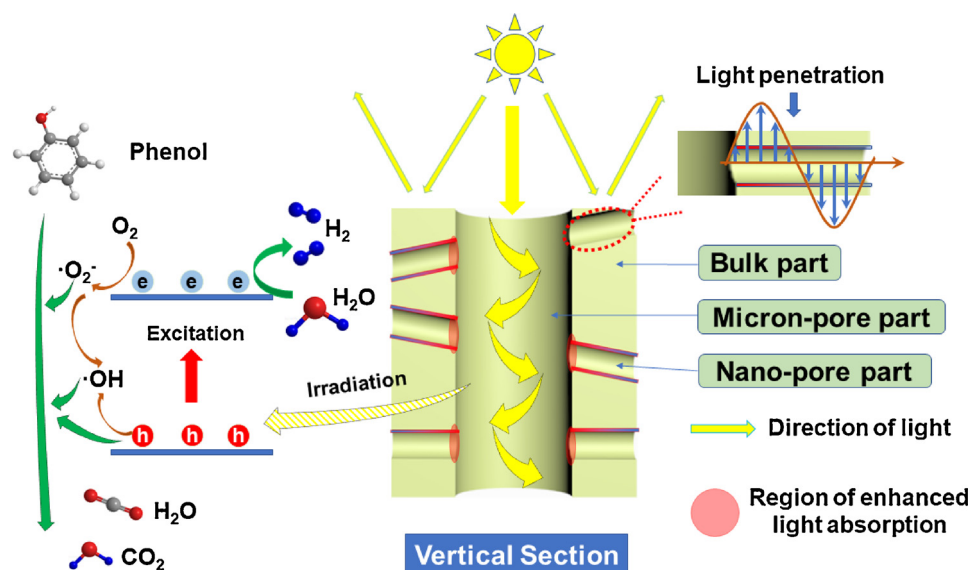

Fig. 9. Possible catalytic mechanism for the FCN material.

The possible mechanisms for H_2 generation and phenol degradation over FCN materials are shown in Fig. 9. Under visible light irradiation, the bulk part on the FCN surface only reflects the light and absorbs a little energy. In contrast, the light wave penetrates the inner structure by multiple reflection inside the 1–2 μm micron-scale pores. Thus, the light energy was absorbed many times. At the same time, the light can be easily transferred to the entrance of nano-scale pores, leading to light absorption inside the catalysts. Besides, this kind of hierarchical pore could enhance light absorption by itself. The catalyst is excited to generate active electrons and holes. The electrons reduce the H^+ to generate H_2 in the photoreduction, and combine with O_2 to form $\cdot O_2^-$, parts of which participate complex reactions to form $\cdot OH$. Meanwhile, the holes take part in the further mineralize the phenol. As for mass transfer, the reactants and products can move freely in the micron-scale pores, and thus the connected nano-scale pores can adsorb more reactants and desorb more products, resulting in better utilization of inner pores. Therefore, the introduction of micron-scale pores not only enhances light absorption in themselves, but also promotes light absorption in the nano-scale pores. Meanwhile, the improved mass transfer and increased reaction area also contribute to the enhancement of photocatalytic efficiency.

and nano-scale pores has been *in situ* prepared by single soft PU template. The use of PU template would not only help to create the hierarchical pore architecture, but also avoid generating carbon residue with a suitable heating rate. The as-prepared FCN materials exhibited highly improved catalytic performances in H_2 generation and phenol degradation under visible light irradiation compared with pristine g-C_3N_4 (PCN). An optical simulation was adopted for the first time to evaluate the effects of a hierarchical pore architecture with micro- and nano-scale pores on the ability of FCN to absorb energy and an explanation for the improved photocatalytic activity based on its enhanced light absorption and penetration ability on the photocatalysts was proposed. Besides, the improved photocatalytic activity performance should be also related with the improved separation efficiency of photo-generated holes and electrons, increased mass transfer, enlarged accessible catalytic area, and enhanced light absorption and penetration, which are all rooted in the hierarchical pore system. The strategy discovered in the work might be widely used for synthesis of hierarchically porous photocatalysts beyond g-C_3N_4. Meanwhile, the optical simulation for evaluating the light absorption and penetration ability could open a door to understand the mechanism of enhanced photocatalytic activity and be meaningful to guide the preparation of some new photocatalysts.

4. Conclusion

To sum up, the hierarchically porous g-C_3N_4 (FCN) with micron-

Acknowledgment

Appendix A. Supplementary data

Supplementary material related to this article can be found, in the online version, at doi:https://doi.org/10.1016/j.apcatb.2018.04.082.

References

[1] M. Liu, Y. Chen, J. Su, J. Shi, X. Wang, L. Guo, Photocatalytic hydrogen production using twinned nanocrystals and an unanchored NiS$_x$ co-catalyst, Nat. Energy 1 (2016) 16151.

[2] H. Xu, J. Yi, X. She, Q. Liu, L. Song, S. Chen, Y. Yang, Y. Song, R. Vajtai, J. Lou, H. Li, S. Yuan, J. Wu, P.M. Ajayan, 2D heterostructure comprised of metallic 1T-MoS$_2$/monolayer O-g-C$_3$N$_4$ towards efficient photocatalytic hydrogen evolution, Appl. Catal. B 220 (2018) 379–385.

[3] J.K. Zhang, Z.B. Yu, Z. Gao, H.B. Ge, S.C. Zhao, C.Q. Chen, S. Chen, X.L. Tong, M.H. Wang, Z.F. Zheng, Y. Qin, Porous TiO$_2$ nanotubes with spatially separated platinum and CoO$_x$ cocatalysts produced by atomic layer deposition for photocatalytic hydrogen production, Angew. Chem. Int. Ed. 56 (2017) 816–820.

[4] J. Huang, Y. He, L. Wang, Y. Huang, B. Jiang, Bifunctional Au@TiO$_2$ core-shell nanoparticle films for clean water generation by photocatalysis and solar evaporation, Energy Convers. Manage. 132 (2017) 452–459.

[5] J.-X. Li, C. Ye, X.-B. Li, Z.-J. Li, X.-W. Gao, B. Chen, C.-H. Tung, L.-Z. Wu, A redox shuttle accelerates O$_2$ evolution of photocatalysts formed in situ under visible light, Adv. Mater. 29 (2017) 1606009.

[6] S. Wang, B.Y. Guan, L. Lu, X.W.D. Lou, Formation of hierarchical In$_2$S$_3$-CdIn$_2$S$_4$ heterostructured nanotubes for efficient and stable visible light CO$_2$ reduction, J. Am. Chem. Soc. 139 (2017) 17305–17308.

[7] M. Zhou, X. Jiang, X. Jiang, K. Xiao, Y. Guo, H. Huang, Z. Lin, J. Yao, C.-H. Tung, L.-Z. Wu, Y. Wu, BaAu$_2$S$_2$: a Au-based intrinsic photocatalyst for high-performance visible-light photocatalysis, Inorg. Chem. 56 (2017) 5173–5181.

[8] W. Che, W. Cheng, T. Yao, F. Tang, W. Liu, H. Su, Y. Huang, Q. Liu, J. Liu, F. Hu, Z. Pan, Z. Sun, S. Wei, Fast photoelectron transfer in (C-ring)-C$_3$N$_4$ plane heterostructural nanosheets for overall water splitting, J. Am. Chem. Soc. 139 (2017) 3021–3026.

[9] Q. Wei, Y. Wang, H. Qin, J. Wu, Y. Lu, H. Chi, F. Yang, B. Zhou, H. Yu, J. Liu, Construction of rGO wrapping octahedral Ag-Cu$_2$O heterostructure for enhanced visible light photocatalytic activity, Appl. Catal. B 227 (2018) 132–144.

[10] Y. Guo, Q. Liu, Z. Li, Z. Zhang, X. Fang, Enhanced photocatalytic hydrogen evolution performance of mesoporous graphitic carbon nitride co-doped with potassium and iodine, Appl. Catal. B 221 (2018) 362–370.

[11] Y. Hu, G. Chen, C. Li, Z. Han, S. Hao, W. Hong, X. Xing, Non-integer induced spontaneous polarization of highly efficient perovskite-based NBTO SCN photocatalysts, J. Mater. Chem. A 5 (2017) 22984–22987.

[12] X. Lang, J. Zhao, X. Chen, Visible-light-induced photoredox catalysis of dye-sensitized titanium dioxide: selective aerobic oxidation of organic sulfides, Angew. Chem. Int. Ed. 55 (2016) 4697–4700.

[13] B. Liu, L.M. Liu, X.F. Lang, H.Y. Wang, X.W. Lou, E.S. Aydil, Doping high-surface-area mesoporous TiO$_2$ microspheres with carbonate for visible light hydrogen production, Energ. Environ. Sci. 7 (2014) 2592–2597.

[14] J. Wang, D. Hao, J. Ye, N. Umezawa, Determination of crystal structure of graphitic carbon nitride: ab lnitio evolutionary search and experimental validation, Chem. Mater. 29 (2017) 2694–2707.

[15] Y. Tang, M. Yuan, B. Jiang, Y. Xiao, Y. Fu, S. Chen, Z. Deng, Q. Pan, C. Tian, H. Fu, Inorganic acid-derived hydrogen-bonded organic frameworks to form nitrogen-rich carbon nitrides for photocatalytic hydrogen evolution, J. Mater. Chem. A 5 (2017) 21979–21985.

[16] Q. Han, B. Wang, Y. Zhao, C. Hu, L. Qu, A graphitic-C$_3$N$_4$ "seaweed" architecture for enhanced hydrogen evolution, Angew. Chem. Int. Ed. 54 (2015) 11433–11437.

[17] Y. Zeng, C. Liu, L. Wang, S. Zhang, Y. Ding, Y. Xu, Y. Liu, S. Luo, A three-dimensional graphitic carbon nitride belt network for enhanced visible light photocatalytic hydrogen evolution, J. Mater. Chem. A 4 (2016) 19003–19010.

[18] J. Li, W. Cui, Y. Sun, Y. Chu, W. Cen, F. Dong, Directional electron delivery via a vertical channel between g-C$_3$N$_4$ layers promotes photocatalytic efficiency, J. Mater. Chem. A 5 (2017) 9358–9364.

[19] X. Wang, J. Chen, X. Guan, L. Guo, Enhanced efficiency and stability for visible light driven water splitting hydrogen production over Cd0.5Zn0.5S/g-C$_3$N$_4$ composite photocatalyst, Int. J. Hydrogen Energy 40 (2015) 7546–7552.

[20] N. Wang, Y. Du, W. Ma, P. Xu, X. Han, Rational design and synthesis of SnO$_2$-encapsulated alpha-Fe$_2$O$_3$ nanocubes as a robust and stable photo-Fenton catalyst, Appl. Catal. B 210 (2017) 23–33.

[21] H. Yu, L. Shang, T. Bian, R. Shi, G.I.N. Waterhouse, Y. Zhao, C. Zhou, L.-Z. Wu, C.-H. Tung, T. Zhang, Nitrogen-doped porous carbon nanosheets templated from g-C$_3$N$_4$ as metal-free electrocatalysts for efficient oxygen reduction reaction, Adv. Mater. 28 (2016) 5080–5086.

[22] L. Yang, J. Huang, L. Shi, L. Cao, H. Liu, Y. Liu, Y. Li, H. Song, Y. Jie, J. Ye, Sb doped SnO$_2$-decorated porous g-C$_3$N$_4$ nanosheet heterostructures with enhanced photocatalytic activities under visible light irradiation, Appl. Catal. B 221 (2018) 670–680.

[23] L. Zhou, Y. Xu, W. Yu, X. Guo, S. Yu, J. Zhang, C. Li, Ultrathin two-dimensional graphitic carbon nitride as a solution-processed cathode interfacial layer for inverted polymer solar cells, J. Mater. Chem. A 4 (2016) 8000–8004.

[24] Q. Han, Z. Cheng, J. Gao, Y. Zhao, Z. Zhang, L. Dai, L. Qu, Mesh-on-mesh graphitic-C$_3$N$_4$@graphene for highly efficient hydrogen evolution, Adv. Funct. Mater. 27 (2017) 1606352.

[25] M. Zhu, S. Kim, L. Mao, M. Fujitsuka, J. Zhang, X. Wang, T. Majima, Metal-free photocatalyst for H$_2$ evolution in visible to near-infrared region: black phosphorus/graphitic carbon nitride, J. Am. Chem. Soc. 139 (2017) 13234–13242.

[26] P. Ye, X. Liu, J. Iocozzia, Y. Yuan, L. Gu, G. Xu, Z. Lin, A highly stable non-noble metal Ni$_2$P co-catalyst for increased H$_2$ generation by g-C$_3$N$_4$ under visible light irradiation, J. Mater. Chem. A 5 (2017) 8493–8498.

[27] P. Wu, J.R. Wang, J. Zhao, L.J. Guo, F.E. Osterloh, Structure defects in g-C$_3$N$_4$ limit visible light driven hydrogen evolution and photovoltage, J. Mater. Chem. A 2 (2014) 20338–20344.

[28] J. Ji, J. Wen, Y. Shen, Y. Lv, Y. Chen, S. Liu, H. Ma, Y. Zhang, Simultaneous non-covalent modification and exfoliation of 2D carbon nitride for enhanced electro-chemiluminescent biosensing, J. Am. Chem. Soc. 139 (2017) 11698–11701.

[29] M. Bellardita, E.I. Garcia-Lopez, G. Marci, I. Krivtsov, J.R. Garcia, L. Palmisano, Selective photocatalytic oxidation of aromatic alcohols in water by using P-doped g-C$_3$N$_4$, Appl. Catal. B 220 (2018) 222–233.

[30] C. Liu, Y. Zhang, F. Dong, A.H. Reshak, L. Ye, N. Pinna, C. Zeng, T. Zhang, H. Huang, Chlorine intercalation in graphitic carbon nitride for efficient photocatalysis, Appl. Catal. B 203 (2017) 465–474.

[31] H. Huang, K. Xiao, N. Tian, F. Dong, T. Zhang, X. Du, Y. Zhang, Template-free precursor-surface-etching route to porous, thin g-C$_3$N$_4$ nanosheets for enhancing photocatalytic reduction and oxidation activity, J. Mater. Chem. A 5 (2017) 17452–17463.

[32] C. Liu, H. Huang, L. Ye, S. Yu, N. Tian, X. Du, T. Zhang, Y. Zhang, Intermediate-mediated strategy to horn-like hollow mesoporous ultrathin g-C$_3$N$_4$ tube with spatial anisotropic charge separation for superior photocatalytic H$_2$ evolution, Nano Energy 41 (2017) 738–748.

[33] N. Tian, Y. Zhang, X. Li, K. Xiao, X. Du, F. Dong, G.I.N. Waterhouse, T. Zhang, H. Huang, Precursor-reforming protocol to 3D mesoporous g-C$_3$N$_4$ established by ultrathin self-doped nanosheets for superior hydrogen evolution, Nano Energy 38 (2017) 72–81.

[34] J. Fu, B. Zhu, C. Jiang, B. Cheng, W. You, J. Yu, Hierarchical porous O-doped g-C$_3$N$_4$ with enhanced photocatalytic CO$_2$ reduction activity, Small 13 (2017) 1603938.

[35] G.S. Liu, S.W. Liu, Q.F. Lu, H.Y. Sun, Z.L. Xiu, Synthesis of mesoporous BiPO$_4$ nanofibers by electrospinning with enhanced photocatalytic performances, Ind. Eng. Chem. Res. 53 (2014) 13023–13029.

[36] Z. Yang, Y.J. Zhang, Z. Schnepp, Soft and hard templating of graphitic carbon nitride, J. Mater. Chem. A 3 (2015) 14081–14092.

[37] Y. Wang, X. Wang, M. Antonietti, Y. Zhang, Facile one-pot synthesis of nanoporous carbon nitride solids by using soft templates, ChemSusChem 3 (2010) 435–439.

[38] J. Zhang, M. Zhang, C. Yang, X. Wang, Nanospherical carbon nitride frameworks with sharp edges accelerating charge collection and separation at a soft photocatalytic interface, Adv. Mater. 26 (2014) 4121–4126.

[39] X. Chen, Y.-S. Jun, K. Takanabe, K. Maeda, K. Domen, X. Fu, M. Antonietti, X. Wang, Ordered mesoporous SBA-15 type graphitic carbon nitride: a semiconductor host structure for photocatalytic hydrogen evolution with visible light, Chem. Mater. 21 (2009) 4093–4095.

[40] Q. Liang, Z. Li, X. Yu, Z.H. Huang, F. Kang, Q.H. Yang, Macroscopic 3D porous graphitic carbon nitride monolith for enhanced photocatalytic hydrogen evolution, Adv. Mater. 27 (2015) 4634–4639.

[41] H. Zhang, L. Zhao, F. Geng, L.-H. Guo, B. Wan, Y. Yang, Carbon dots decorated graphitic carbon nitride as an efficient metal-free photocatalyst for phenol degradation, Appl. Catal. B 180 (2016) 656–662.

[42] J. Zhang, M. Zhang, G. Zhang, X. Wang, Synthesis of carbon nitride semiconductors in sulfur flux for water photoredox catalysis, ACS Catal. 2 (2012) 940–948.

[43] J. Xu, H. Wang, C. Zhang, X. Yang, S. Cao, J. Yu, M. Shalom, From millimeter to subnanometer: vapor-solid deposition of carbon nitride hierarchical nanostructures directed by supramolecular assembly, Angew. Chem. Int. Ed. 56 (2017) 8426–8430.

[44] X.C. Wang, J.C. Yu, C.M. Ho, Y.D. Hou, X.Z. Fu, Photocatalytic activity of a hierarchically macro/mesoporous titania, Langmuir 21 (2005) 2552–2559.

[45] W. Ma, N. Wang, Y. Fan, T. Tong, X. Han, Y. Du, Non-radical-dominated catalytic degradation of bisphenol A by ZIF-67 derived nitrogen-doped carbon nanotubes frameworks in the presence of peroxymonosulfate, Chem. Eng. J. 336 (2018) 721–731.

[46] L. Wang, X. Duan, G. Wang, C. Liu, S. Luo, S. Zhang, Y. Zeng, Y. Xu, Y. Liu, X. Duan, Omnidirectional enhancement of photocatalytic hydrogen evolution over hierarchical "cauline leaf" nanoarchitectures, Appl. Catal. B 186 (2016) 88–96.

[47] Q. Zhang, J. Deng, Z. Xu, M. Chaker, D. Ma, High-efficiency broadband C$_3$N$_4$ photocatalysts: synergistic effects from upconversion and plasmons, ACS Catal. 7 (2017) 6225–6234.

[48] Y. Li, Y. Jiang, Z. Ruan, K. Lin, Z. Yu, Z. Zheng, X. Xu, Y. Yuan, Simulation-guided synthesis of graphitic carbon nitride beads with 3D interconnected and continuous meso/macropore channels for enhanced light absorption and photocatalytic performance, J. Mater. Chem. A 5 (2017) 21300–21312.

[49] C. Branca, C. Di Blasi, A. Casu, V. Morone, C. Costa, Reaction kinetics and morphological changes of a rigid polyurethane foam during combustion, Thermochim.

Acta 399 (2003) 127–137.

[50] S.S. Dosanjh, P.J. Pagni, A.C. Fernandezpello, Forced cocurrent smoldering combustion, Combust. Flame 68 (1987) 131–142.

[51] C. Ye, X.-Z. Wang, J.-X. Li, Z.-J. Li, X.-B. Li, L.-P. Zhang, B. Chen, C.-H. Tung, L.-Z. Wu, Protonated graphitic carbon nitride with surface attached molecule as hole relay for efficient photocatalytic O_2 evolution, ACS Catal. 6 (2016) 8336–8341.

[52] Y. Wang, W. Yang, X. Chen, J. Wang, Y. Zhu, Photocatalytic activity enhancement of core-shell structure g-C_3N_4@TiO_2 via controlled ultrathin g-C_3N_4 layer, Appl. Catal. B 220 (2018) 337–347.

[53] G.P. Mane, S.N. Talapaneni, K.S. Lakhi, H. Ilbeygi, U. Ravon, K. Al-Bahily, T. Mori, D.-H. Park, A. Vinu, Highly ordered nitrogen-rich mesoporous carbon nitrides and their superior performance for sensing and photocatalytic hydrogen generation, Angew. Chem. Int. Ed. 56 (2017) 8481–8485.

[54] J.-W. Zhang, S. Gong, N. Mahmood, L. Pan, X. Zhang, J.-J. Zou, Oxygen-doped nanoporous carbon nitride via water-based homogeneous supramolecular assembly for photocatalytic hydrogen evolution, Appl. Catal. B 221 (2018) 9–16.

[55] Y. Li, X. Xu, Y. He, Y. Jiang, K. Lin, Nitrogen doped macroporous carbon as electrode materials for high capacity of supercapacitor, Polymers 9 (2017) 2.

[56] Y. He, P. Xu, B. Zhang, Y. Du, B. Song, X. Han, H. Peng, Ultrasmall MnO nanoparticles supported on nitrogen-doped carbon nanotubes as efficient anode materials for sodium ion batteries, ACS Appl. Mater. Inter. 9 (2017) 38401–38408.

[57] Y. Yu, W. Yan, W. Gao, P. Li, X. Wang, S. Wu, W. Song, K. Ding, Aromatic ring substituted g-C_3N_4 for enhanced photocatalytic hydrogen evolution, J. Mater. Chem. A 5 (2017) 17199–17203.

[58] A. Zada, M. Humayun, F. Raziq, X. Zhang, Y. Qu, L. Bai, C. Qin, L. Jing, H. Fu, Exceptional visible-light-driven cocatalyst-free photocatalytic activity of g-C_3N_4 by well designed nanocomposites with plasmonic Au and SnO_2, Adv. Energy Mater. 6 (2016) 1601190.

[59] G.S. Liu, S.J. You, M. Ma, H. Huang, N.Q. Ren, Removal of nitrate by photocatalytic denitrification using nonlinear optical material, Environ. Sci. Technol. 50 (2016) 11218–11225.

[60] G.S. Liu, S.J. You, Y. Tan, N.Q. Ren, In situ photochemical activation of sulfate for enhanced degradation of organic pollutants in water, Environ. Sci. Technol. 51 (2017) 2339–2346.

[61] G. Zhang, A. Savateev, Y. Zhao, L. Li, M. Antonietti, Advancing the n -& pi* electron transition of carbon nitride nanotubes for H_2 photosynthesis, J. Mater. Chem. A 5 (2017) 12723–12728.

[62] R. Godin, Y. Wang, M.A. Zwijnenburg, J. Tang, J.R. Durrant, Time-resolved spectroscopic investigation of charge trapping in carbon nitrides photocatalysts for hydrogen generation, J. Am. Chem. Soc. 139 (2017) 5216–5224.

[63] X. Wang, Y. He, G. Cheng, L. Shi, X. Liu, J. Zhu, Direct vapor generation through localized solar heating via carbon-nanotube nanofluid, Energy Convers. Manage. 130 (2016) 176–183.

[64] L. Shi, Y. He, Y. Huang, B. Jiang, Recyclable Fe_3O_4@CNT nanoparticles for high-efficiency solar vapor generation, Energy Convers. Manage. 149 (2017) 401–408.

[65] J. Huang, Y. He, M. Chen, B. Jiang, Y. Huang, Solar evaporation enhancement by a compound film based on Au@TiO_2 core–shell nanoparticles, Sol. Energy 155 (2017) 1225–1232.

[66] F. Wang, Z. Cheng, J. Tan, Y. Yuan, Y. Shuai, L. Liu, Progress in concentrated solar power technology with parabolic trough collector system: a comprehensive review, Renew. Sust. Energy Rev. 79 (2017) 1314–1328.

[67] Q. Mao, Recent developments in geometrical configurations of thermal energy storage for concentrating solar power plant, Renew. Sust. Energy Rev. 59 (2016) 320–327.

[68] Q. Mao, H. Chen, Y. Zhao, H. Wu, A novel heat transfer model of a phase change material using in solar power plant, Appl. Therm. Eng. 129 (2018) 557–563.

[69] Y. Li, Y. Feng, X. Sun, Y. He, A sodium-ion-conducting direct formate fuel cell: generating electricity and producing base, Angew. Chem. Int. Ed. 56 (2017) 5734–5737.

[70] L. Yang, Y. Xuan, Y. Han, J. Tan, Investigation on the performance enhancement of silicon solar cells with an assembly grating structure, Energy Convers. Manage. 54 (2012) 30–37.

[71] H. Duan, Y. Xuan, Enhanced optical absorption of the plasmonic nanoshell suspension based on the solar photocatalytic hydrogen production system, Appl. Energy 114 (2014) 22–29.

[72] Z.-H. Ruan, Y. Yuan, X.-X. Zhang, Y. Shuai, H.-P. Tan, Determination of optical properties and thickness of optical thin film using stochastic particle swarm optimization, Sol. Energy 127 (2016) 147–158.

[73] T.-T. Zhuang, Y. Liu, Y. Li, Y. Zhao, L. Wu, J. Jiang, S.-H. Yu, Integration of semiconducting sulfides for full-spectrum solar energy absorption and efficient charge separation, Angew. Chem. Int. Ed. 55 (2016) 6396–6400.

[74] Y. Yuan, Z.-H. Ruan, X. Huang, Y.-Q. Jiang, H.-P. Tan, Energy-absorption-based explanation of the TiO_2/C photocatalytic activity enhancement mechanism, J. Catal. 348 (2017) 246–255.

[75] H. Zhang, X. Gu, P. Liu, J. Song, J. Cheng, H. Su, Highly efficient visible-light-driven catalytic hydrogen evolution from ammonia borane using non-precious metal nanoparticles supported by graphitic carbon nitride, J. Mater. Chem. A 5 (2017) 2288–2296.

[76] M.Z. Rahman, P.C. Tapping, T.W. Kee, R. Smernik, N. Spooner, J. Moffatt, Y. Tang, K. Davey, S.-Z. Qiao, A benchmark quantum yield for water photoreduction on amorphous carbon nitride, Adv. Funct. Mater. 27 (2017) 1702384.

[77] J. Zhang, F. Guo, X. Wang, An optimized and general synthetic strategy for fabrication of polymeric carbon nitride nanoarchitectures, Adv. Funct. Mater. 23 (2013) 3008–3014.

[78] J. Ran, T.Y. Ma, G. Gao, X.-W. Du, S.Z. Qiao, Porous P-doped graphitic carbon nitride nanosheets for synergistically enhanced visible-light photocatalytic H_2 production, Energy Environ. Sci. 8 (2015) 3708–3717.

[79] J. Hong, X. Xia, Y. Wang, R. Xu, Mesoporous carbon nitride with in situ sulfur doping for enhanced photocatalytic hydrogen evolution from water under visible light, J. Mater. Chem. 22 (2012) 15006–15012.

[80] H. Huang, Y. He, X. Li, M. Li, C. Zeng, F. Dong, X. Du, T. Zhang, Y. Zhang, $Bi_2O_2(OH)(NO3)$ as a desirable $[Bi_2O_2]^{2+}$ layered photocatalyst: strong intrinsic polarity, rational band structure and {001} active facets co-beneficial for robust photooxidation capability, J. Mater. Chem. A 3 (2015) 24547–24556.

[81] H. Huang, S. Tu, C. Zeng, T. Zhang, A.H. Reshak, Y. Zhang, Macroscopic polarization enhancement promoting photo- and piezoelectric-induced charge separation and molecular oxygen activation, Angew. Chem. Int. Ed. 56 (2017) 11860–11864.

[82] H. Huang, X. Li, J. Wang, F. Dong, P.K. Chu, T. Zhang, Y. Zhang, Anionic group self-doping as a promising strategy: band-gap engineering and multi-functional applications of high-performance CO_3^{2-}-doped $Bi_2O_2CO_3$, ACS Catal. 5 (2015) 4094–4103.